Precipitation Behaviors in Al-Cu-Mg and 2024 Aluminum Alloys

HAN-CHENG SHIH, NEW-JIN HO, and J.C. HUANG

The precipitation behaviors and aging reactions of the pseudobinary Al-Cu-Mg alloy and the commercial 2024 alloy under unstretched and stretched conditions have been investigated in this study by means of conductivity and hardness measurements, differential scanning calorimetry, and transmission electron microscopy (TEM). The morphologies and growth modes of various defects and transition phases as well as the interaction among them were widely discussed. In particular, an electron diffraction ring pattern was found to correspond to the axial growth of the GPB2 zone. This suggested that the atom groups constructing this cylindrical zone are statistically, uniformly arranged in the adjacent $\{100\}_{Al}$ planes and the GPB2 zone is only a partially ordered version of the GPB zone in $\langle 001 \rangle_{Al}$ directions. Moreover, few GPB2 zones can survive long time overaging due to the Gibbs–Thomson effect. As for the S' precipitates, they preferentially nucleate on dislocations. During subsequent growth, they can further coalesce into two morphologies (corrugated sheets and wide plates) for the unstretched specimens. However, for the stretched specimens, this coalescing process does not occur until a long time of overaging due to more introduced dislocations. Therefore, the rate of Ostward ripening decreases and the peak hardness becomes flattened. Finally, based on the present analyses, the aging sequence of the two alloys studied could be revised with respect to previous investigations and their isothermal aging reactions can be subdivided into five main stages. These stages correspond to (1) GPB zone precipitation, (2) fast *in situ* precipitation of GPB2 zones from GPB zones and their subsequent growth, (3) fast nucleation and accelerating growth of the S' phase, (4) decelerating growth of the S' phase, and (5) Ostward ripening of the S' and S phases, respectively.

I. INTRODUCTION

HIGH specific strength, good fracture toughness, and excellent fatigue properties are particularly required for precipitation-hardened aluminum alloys for aircraft applications. To fulfill these requirements, a few technological methods have been tentatively used by changing solute content,[1,2,3] adding impurity elements,[4–8] and employing a thermomechanical treatment.[9,10,11] Among them, increasing the contents of appropriate alloying elements and/or applying a final thermomechanical treatment (FTMT) has been recognized to be the most prevalent way. For example, it has been qualitatively shown that for the Al-Cu-Mg alloys, increasing the contents of Cu and Mg would enhance the precipitation of the strengthening phase (S'), while cold stretching prior to any aging treatment would render this phase shorter and thinner in size and denser in distribution.[12] However, the dependence of the morphologies and growth modes of various transition phases (*e.g.*, GPB2 zones and the S' phase) on these two metallurgical treatments has been paid little attention thus far. On the other hand, the evolution of these transition phases during aging has been widely examined using transmission electron microscopy (TEM),[5–7,12] X-ray, and hardness studies.[13–16] However, the measurements of specific resistivity[17,18] or electrical conductivity[19,20] (EC) and differential scanning

calorimetry (DSC)[21] have been shown recently to be effective methods to provide further evidence associated with the variation in the quantity of precipitates. Therefore, the combination of these techniques is believed to afford giving a more comprehensive insight into the precipitation behaviors of materials.

With respect to these experimental techniques, the increase or decrease in conductivity is generally used to follow the precipitation or redissolution process of excess solutes.[20] However, it must be noticed that the precipitation of GP zones can conversely result in a decrease in conductivity because their sizes are at the scale of the mean free path of electrons.[22] Besides, the effects of the microstructural modifications such as vacancies, dislocations, and the precipitate morphology also require to be unambiguously evaluated. In the DSC studies, the variation of relative contents of various transition phases can be identified because the endothermic and exothermic peaks in DSC thermograms signify the dissolution of pre-existing phases and the precipitation of excess solutes during DSC scanning, respectively. In other words, the larger endothermic or smaller exothermic peak always suggests that more precipitates pre-exist within the matrix. The area of the peak also was found to be proportional to the volume fraction of precipitates.[23] Moreover, it has been widely shown that the acceleration of the precipitation rate results in the shift of the exothermic peaks to lower temperatures, while the deceleration of the dissolution rate (stabilization) results in the shift of the endothermic peaks to higher temperatures.

In this study, the techniques of EC, hardness, DSC, and TEM were used together to investigate the precipitation behavior during aging of the pseudobinary Al-Cu-Mg alloy

Table I. Chemical Compositions of Two Aluminum Alloys (Weight Percent)

Alloy	Cu	Mg	Si	Fe	Mn	Zn	Cr	Ti	Ni	Al
Al-Cu-Mg	2.62	1.35	0.000	0.009	0.00	0.007	0.002	0.005	0.002	balance
2024	3.98	1.38	0.099	0.210	0.55	0.019	0.005	0.019	0.003	balance

and the 2024 alloy in the unstretched and stretched conditions. The morphologies and growth modes of various defects and transition phases as well as the interaction among them will be widely discussed. As a result, the isothermal aging reactions of these two alloys can be revised with respect to previous investigations.[13,14]

II. EXPERIMENTAL PROCEDURES

The materials used in this investigation were the pseudobinary Al-Cu-Mg alloy and the commercial 2024 alloy with the chemical compositions listed in Table I. They were DC-cast, homogenized at 480 ± 3 °C for 48 hours, then hot- and cold-rolled into sheets of 4-mm thickness. These cold-rolled sheets were cut into strips 200-mm long and 40-mm wide. After solid-solution treatment at 495 ± 3 °C for 1 hour and quenching into room-temperature water, some strips were immediately stretched to 1.5 pct strain at room temperature with a MTS machine. These stretched strips, together with the unstretched ones, were then rapidly dipped into a container filled with liquid nitrogen to prevent the occurrence of any aging. Subsequently, shortly after cutting these unstretched and stretched strips into specimens 50-mm long × 40-mm wide × 4-mm thick, many sets of specimens, each set containing one unstretched and one stretched specimen, were simultaneously aged in an oil bath at 170 °C ± 1 °C and a salt bath at 190 °C or 240 °C ± 3 °C, respectively. They were then taken out of these two baths at a predetermined period, ranging from 5 seconds to 30 days and requenched into room-temperature water. The maximum duration at room temperature between solid solution quenching and artificial aging was <15 minutes, during which the effect of natural aging was not significant.[19,20]

Electrical conductivity and hardness measurements were made at room temperature on these aged specimens immediately after artificial aging. The instrument used was the NORTEC* NDT-17 eddy current tester and the Wilson In-

---

*NORTEC is a trademark of Staveley NDT Technologies, Inc., East Hartford, CT.

---

strument 3TT hardness tester, respectively. The measured units were the percentage of International Annealed Copper Standard (IACS) calibrated at 20 °C and the Rockwell B scale (R_B), respectively.

The DSC measurement was conducted in a Du Pont 9900 thermal analysis system equipped with a DSC cell through which an Ar atmosphere was passed to minimize oxidation. Before any measurements were made, the cell was calibrated by an indium standard, the only reaction peak of which is at 156.4 °C, the associated endothermic energy being 28.42 J/g. Therefore, the cell constant of 1.179 could be obtained accurately. To reduce the transient phenomenon at the beginning of the DSC run, 99.99 pct purity aluminum discs similar in mass to the current samples were taken as

the reference. Disclike samples and references samples of about 120 mg (6.5 mm in diameter × 1.5 mm in thickness) were then separately placed on the DSC platforms and scanned at a heating rate of 10 °C/min in the temperature range from 30 °C to 550 °C.

Thin foils with a thickness of about 70 μm were prepared and hand ground from the bulk specimens (t = 4 mm) for electrical conductivity and hardness measurements. Disc samples of 3 mm in diameter were then punched from these foils and further thinned up to perforation by twin-jet polishing in a solution consisting of one part nitric acid and three parts methyl alcohol at 15 V. They were finally rinsed in reagent-grade methanol and distilled water and subsequently examined in a JEOL* 100CX TEM equipped with

---

*JEOL is a trademark of Japan Electron Optics Ltd., Tokyo.

---

a double-tilt stage, operated at 100 kV.

III. RESULTS

A. Electrical Conductivity and Hardness Measurement

1. Unstretched pseudobinary Al-Cu-Mg alloy

Figure 1 shows the variations of the electrical conductivity and hardness as a function of logarithmic aging time at different holding temperatures for the unstretched specimens of the Al-Cu-Mg alloy. The initial descending and leveling portions of the conductivity curves are outlined with the dashed lines, the sigmoidal portion with the solid lines. From this figure, the conductivity and hardness values immediately after quenching were found to be 40 pct IACS and 34.2 R_B, respectively. With increasing the aging time to 30 seconds, the conductivity value decreases to 37.5, 38.2, and 38.8 pct IACS, while the hardness value increases to 51.1, 50.5, and 39.4 R_B, for the holding temperatures of 170 °C, 190 °C, and 240 °C, respectively. The conductivity and hardness then roughly level off for a period that is about 12, 1, and 0.08 hours for the holding temperatures of 170 °C, 190 °C, and 240 °C, respectively. Subsequently, the conductivity rises along a sigmoidal-type curve and approaches a saturation value of 52 pct IACS, irrespective of aging temperatures. In contrast, the hardness rises to a peak value, followed by a final decrease due to overaging. The peak hardness values obtained were found to be about 69, 66, and 63 R_B, for the holding temperatures of 170 °C, 190 °C, and 240 °C, respectively. The time required for achieving these peak hardnesses was also found to be about 64, 12, and 0.75 hours, exhibiting a decrease with increasing the aging temperature.

2. Stretched pseudobinary Al-Cu-Mg alloy

The shapes of the conductivity and hardness curves for the stretched specimens resemble those for the unstretched specimens, as shown in Figure 2. The conductivity and hardness values of the stretched specimens in the as-quenched state were found to be 39.2 pct IACS and 43 R_B,
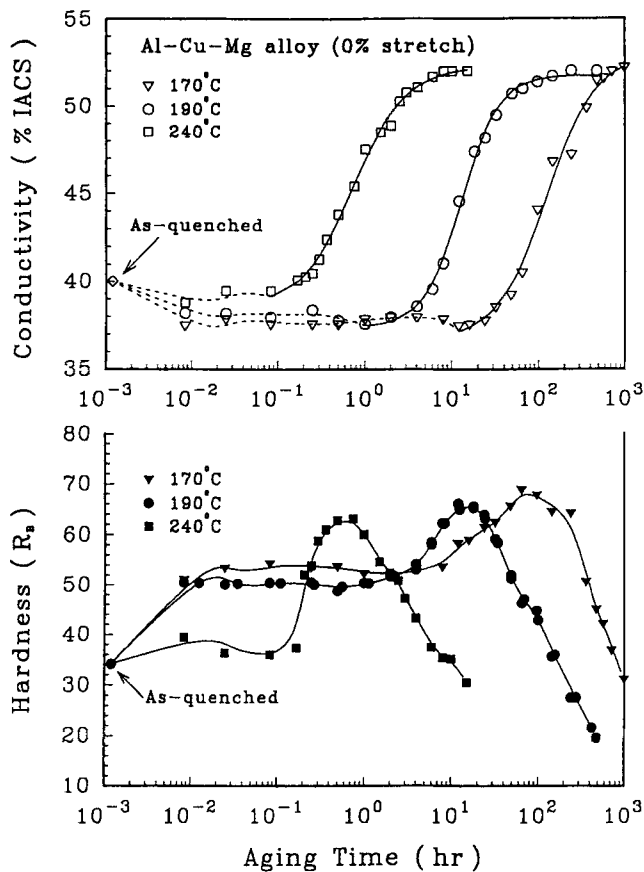
Fig. 1—Eddy current conductivity and Rockwell B hardness vs aging time at three holding temperatures for the unstretched specimens of the pseudobinary Al-Cu-Mg alloy.
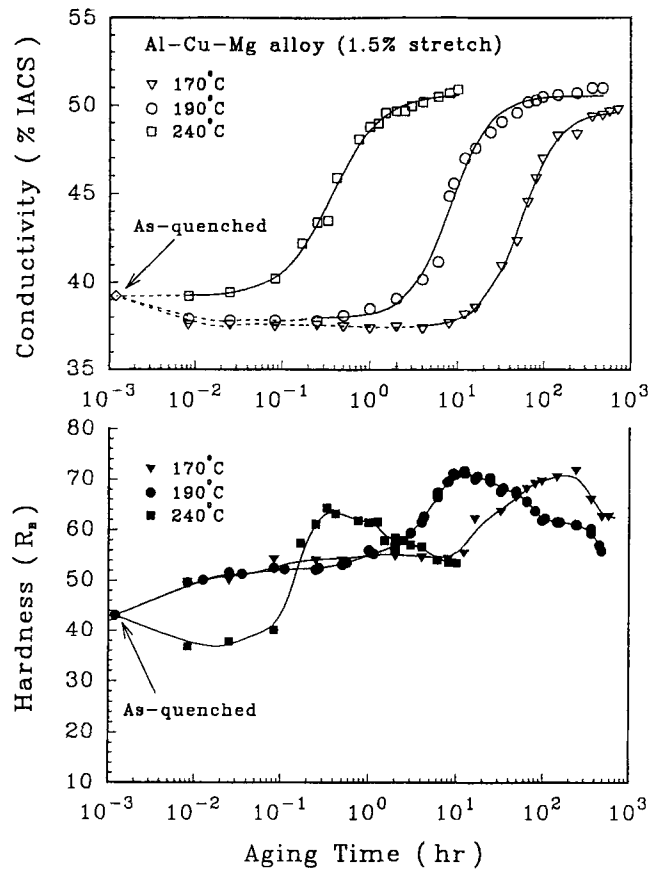

Fig. 2—Eddy current conductivity and Rockwell B hardness vs aging time at three holding temperatures for the stretched (1.5 pct preaging strain) specimens of the pseudobinary Al-Cu-Mg alloy.

which are lower by 0.8 pct IACS and higher by 8.8 R_B than those of the unstretched specimens, respectively. However, the differences in the conductivity and hardness between the unstretched and stretched specimens aged at each of the aging temperatures rapidly diminish within the aging time of 30 seconds, and become not obvious after the conductivity and hardness curves enter the leveling portions. This reduces the rates of both the initial decrease in conductivity and the initial increase in hardness. The phenomenon of the initial drop in the hardness was even observed at the aging temperature of 240 °C. Moreover, the time over the leveling portions of the conductivity curves was found to be about 4, 0.25, and 0.008 hours for the holding temperatures of 170 °C, 190 °C, and 240 °C, respectively, exhibiting a decrease due to preage stretching. The commencement of the sigmoidal portion of the conductivity curves and the corresponding rise of the hardness curves thus occur at a shorter time for the stretched specimens than the unstretched ones. Also, the time required for achieving the peak hardness decreases for the stretched specimens, especially at higher aging temperatures. On the other hand,the peak hardness value of the stretched specimens increases to 71.8, 71.7, and 64.3 R_B for the holding temperatures of 170 °C, 190 °C, and 240 °C, respectively. Furthermore, the hardness around the peak is flattened and the overaging rate is alleviated for the stretched specimens. The conductivity of the stretched specimens was also found to approach a saturation value of 51 pct IACS, which is lower only by 1 pct IACS

than that of the unstretched specimens, though somewhat longer aging time was required for the stretched specimens aged at 170 °C.

3. Unstretched and stretched 2024 alloys

For the 2024 alloy, as shown in Figure 3, the conductivity of the unstretched specimens in the as-quenched state (32 pct IACS) is apparently lower by 8 pct IACS, while the corresponding hardness (53 R_B) is prominently higher by 18.8 R_B than those of the Al-Cu-Mg alloy. When the conductivity and hardness curves enter the leveling portions within the aging time of 30 seconds, the initial conductivity value of the unstretched specimens of the 2024 alloy decreases to 30.6, 30.9, and 31.4 pct IACS, while the corresponding hardness value increases to 67.4, 70.1, and 61.9 R_B, for the holding temperatures of 170 °C, 190 °C, and 240 °C, respectively. Subsequently, the time over the leveling portions of the conductivity curves was found to be about 4, 0.5, and 0.025 hours, for the holding temperatures of 170 °C, 190 °C, and 240 °C, respectively. As compared with the conductivity curves of the unstretched specimens of the Al-Cu-Mg alloy (Figure 1), this shows that the sigmoidal portion of the conductivity curves of the 2024 alloy commences at a shorter time. However, the slope of the sigmoidal portions of the 2024 alloy is smaller than that of the Al-Cu-Mg alloy. As a result, the inflections of the sigmoidal portions of the 2024 alloy aged at the higher temperatures of 190 °C and 240 °C do not shift toward the side of shorter aging time. On the other hand, the peak hardness
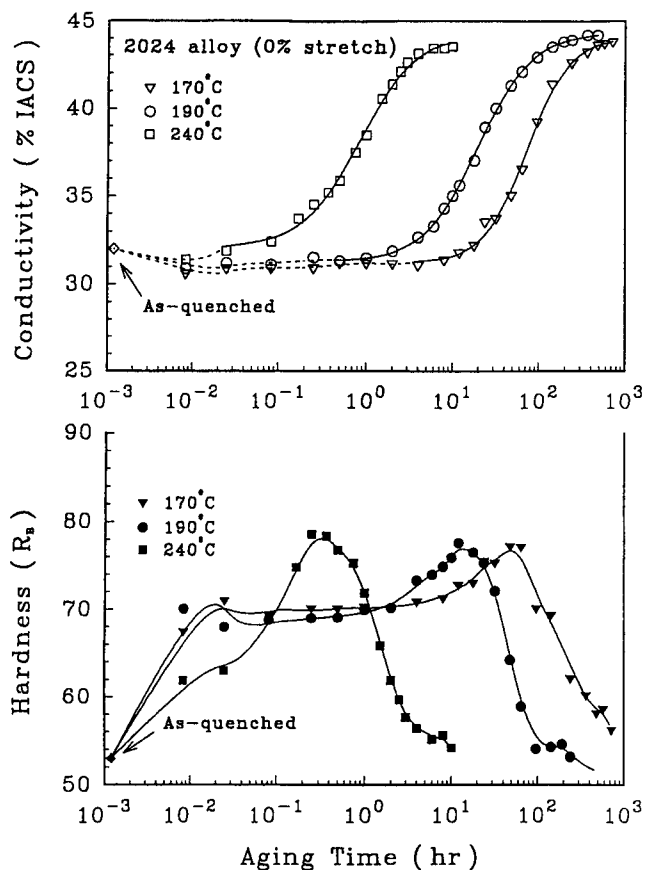
Fig. 3—Eddy current conductivity and Rockwell B hardness vs aging time at three holding temperatures for the unstretched specimens of the commercial 2024 aluminum alloy.
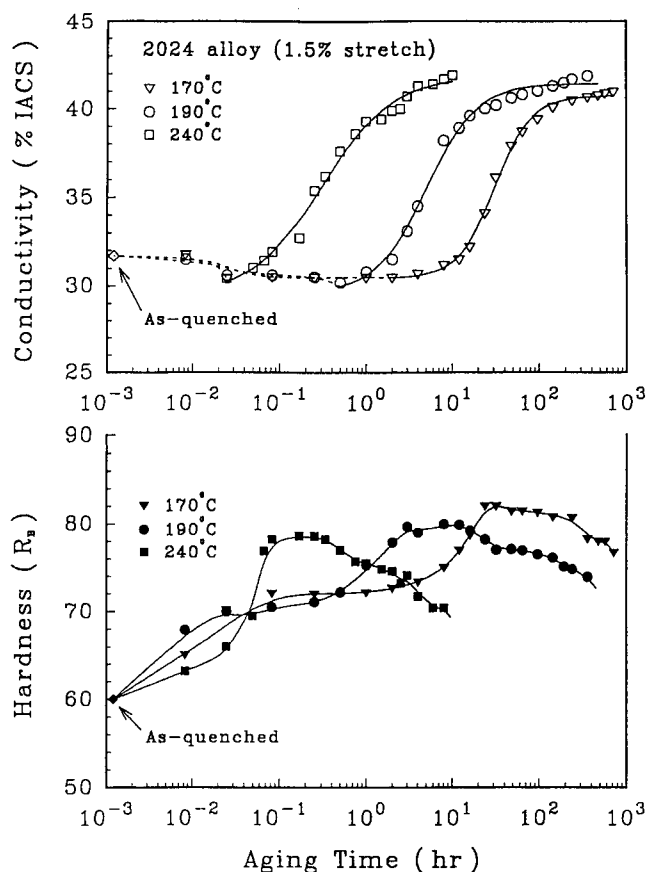

Fig. 4—Eddy current conductivity and Rockwell B hardness vs aging time at three holding temperatures for the stretched (1.5 pct preaging strain) specimens of the commercial 2024 aluminum alloy.

values at the three aging temperatures studied increase to about 78 R_B for the 2024 alloy. However, the time required for achieving these peak hardnesses was found to be about 48, 12, and 0.25 hours for the holding temperatures of 170 °C, 190 °C, and 240 °C, respectively. This is shorter than that of the Al-Cu-Mg alloy. Finally, the conductivity of the unstretched specimens of the 2024 alloy was also found to approach a saturation value of 44 pct IACS, which is lower by 8 pct IACS than that of the Al-Cu-Mg alloy.

The trend in the change of conductivity and hardness between the unstretched and stretched specimens of the 2024 alloy is similar to that of the Al-Cu-Mg alloy, as shown in Figures 3 and 4. However, the conductivity and hardness curves obviously shift toward the side of shorter aging time for the stretched specimens of the 2024 alloy. The phenomenon that the hardness around the peak flattens for the stretched specimens of the Al-Cu-Mg alloy can also be found and is even more prominent for those of the 2024 alloy, (compare Figure 2 with 4).

B. *Differential Scanning Calorimetry*

To realize the precipitation behavior of the Al-Cu-Mg alloys, the specimens for conductivity and hardness measurements were made into DSC samples. Figure 5 shows a typical DSC thermogram for the specimens of the Al-Cu-Mg alloy. Curves 1 through 6 are for the unstretched specimens aged for various aging time at 190 °C, while curve 7 is for the stretched specimen aged for 12 hours at 190

°C. In curve 1 (as-quenched state), five peaks can be identified, which are associated with the GPB zone precipitation (A peak), the GPB zone dissolution (B peak), the GPB2 zone or the S″ phase dissolution (C peak), the S′ (S) phase precipitation (D peak), and the S phase dissolution (E peak), as suggested by Jena et al.[21] However, no definite peak for the precipitation of GPB2 zones (or the S″ phase) and the S phase could be appreciated, implying the in situ transformation of GPB into GPB2 zones (or the S″ phase) and the S′ into S phase. On the other hand, the B and C peaks were seen to overlap with each other, but the E peak did not to correspond separably to the dissolution of the S′ and S phases. This also implies that the structure of GPB zones is almost similar to that of GPB2 zones (or the S″ phase). However, the S′ phase is not easily distinguishable in structure from the S phase and therefore both are sometime considered as a single phase, i.e., the S′ (S) phase.

Following the course of aging at 190 °C, the A and B peaks of curve 2 disappear, whereas the C peak somewhat shifts to a higher temperature. This shows that within the aging time of 1.5 min, GPB zones rapidly precipitate and then in situ transform into GPB2 zones which subsequently begin to grow. At this time, the aging stage is corresponding to the observed initial decrease of the conductivity curve. After aging for a longer time, the area of the C peak gradually increases and its peak position shifts to higher temperatures (curves 1 through 3), meaning that more GPB2 zones precipitate and then grow to larger sizes. As comparing curves 2 and 3, the area of the D peak com-
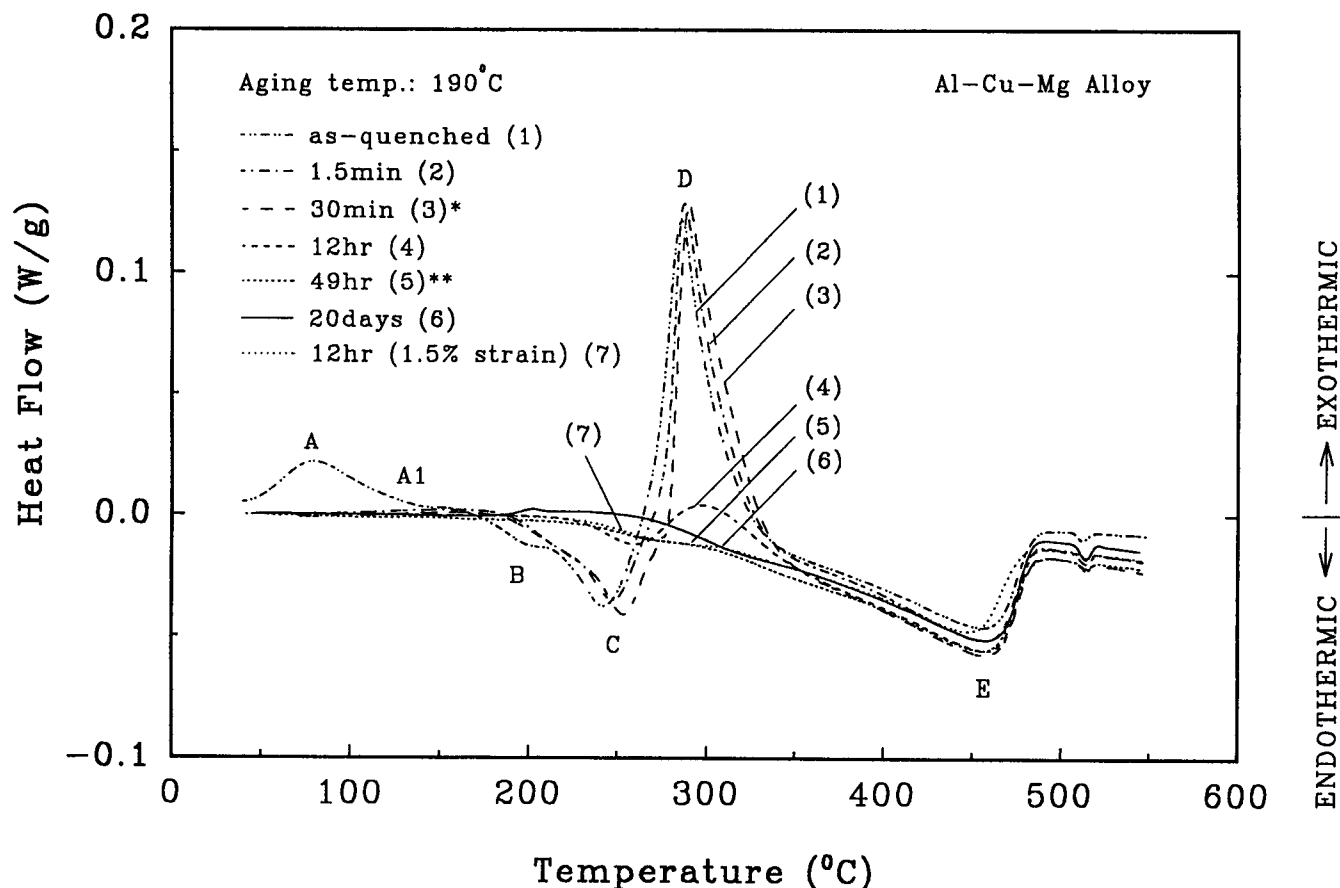
Fig. 5—DSC thermograms (heat rate: 10 °C/min) for the unstretched specimens and one stretched (1.5 pct preaging strain) specimen of the pseudobinary Al-Cu-Mg alloy aged at 190 °C for various times (* and ** correspond to the onset and finishing of the precipitation of the S' phase, respectively).

mences to decrease at 30 minutes, indicating the initial precipitation of the S' phase. The S' precipitation then accelerates until about 12 hours because the area of the D peak largely reduces before this time (curve 4) and then gradually slows down at much longer aging time. After 49 hours, GPB2 zones (or the S" phase) were surprisingly found to still survive in small amounts even though the precipitation of the S' phase has finished and the *in situ* transformation of the S' into S phases has been progressing (compare C peaks in curves 5 (49 hours) and 6 (20 days)). Moreover, for the same aging time, the D peak of curve 7 completely disappears in contrast with that of curve 4, revealing the acceleration of the S' precipitation due to preage stretching.

C. Transmission Electron Microscopy

The effects of aging conditions and preage stretching on the microstructure are mainly illustrated by microscopic observations for the Al-Cu-Mg alloy aged at 190 °C for various times. Some samples of the 2024 alloy are also examined for comparisons.

1. *Pseudobinary Al-Cu-Mg alloy*
a. Initial aging
Figure 6(a) shows TEM bright-field micrographs of the unstretched Al-Cu-Mg alloy aged for 30 minutes at 190 °C. The aging stage corresponds to the leveling portion of the conductivity curve. The microstructure consists of dislocation loops, helixlike dislocations, and a mottled back-

ground structure. Sometimes, paired dislocation loops could also be observed to exist individually at other places of samples (Figure 6(b)). Some of these loops (shown by single arrow) lie on the planes parallel to the electron beam direction ($z \approx [001]$), while the others (elliptical shape, shown by double arrow) lie on the planes at 45 deg to both the beam direction and a $\langle 100 \rangle_{Al}$ direction (the major axis is about twice as long as the minor axis). Obviously, they all lie on various $\{110\}_{Al}$ planes. Therefore, the helixlike dislocation in Figure 6(a) is actually made up of the individual dislocation loops which overlap on the adjacent $\{110\}_{Al}$ planes. Additionally, these helixlike or paired dislocation loops also were seen to be in close contact with the mottle points (Figure 6).

With increasing the aging time to 1 hour (or raising the temperature), as shown in Figure 7(a), the radii of these dislocation loops grow much larger and their numbers become, relatively fewer. Meanwhile, as shown in Figure 7(c), weak and orthogonal diffraction streaks were found to center at $\langle 110 \rangle_{Al}$ g vectors of the electron diffraction pattern. These characteristic diffraction streaks reveal the initial precipitation of the S' phase in terms of the d-spacings of the reflection planes (Figure 8). Although the intensity of the orthogonal streaks is too weak to show the image of very tiny S' precipitates, the weak beam dark field (WBDF) image of the dislocation lines taken near $[020]_{Al}$ g vector, as shown in Figure 7(b), exhibits that these lines are discontinuous, in contrast to their corresponding bright field image in Figure 7(a), where the morphology of the dislocation
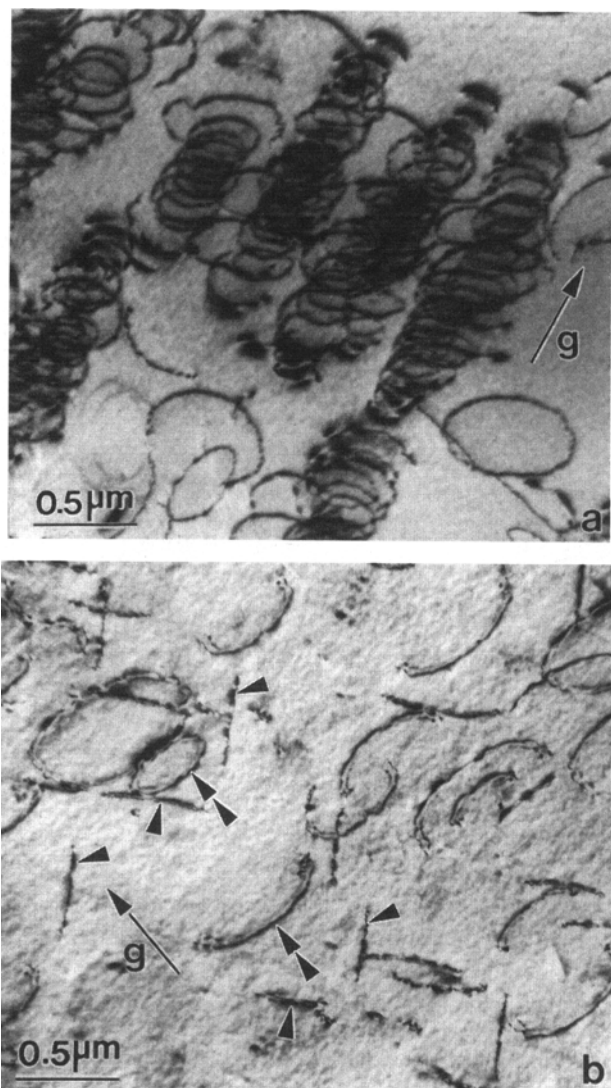
Fig. 6—Microstructure of the unstretched pseudobinary Al-Cu-Mg alloy aged at 190 °C for 30 min: (*a*) bright-field TEM micrograph (**g** = [0$\bar{2}$0], *z* ≈ [101]), showing dislocation loops and helixlike dislocations in the {100} planes; and (*b*) bright-field TEM micrograph (**g** = [020], *z* ≈ [001]), showing paired dislocation loops lying on various orientations of {110}$_{Al}$ planes. The loops lying on the planes parallel to the beam direction are indicated with single arrows, while those lying on the planes at 45 deg to both the beam direction and a ⟨100⟩$_{Al}$ direction are indicated with double arrows. The matrix shows a mottled background.

lines is continuous. This points out the fact that these dislocation lines were decorated intermittently with some tiny precipitates (*e.g.*, S'), similarly to that observed by Chandler and Bee.[24]

Moreover, as shown in Figure 7(c), the diffraction pattern taken near ⟨001⟩$_{Al}$ zone axes exhibits the existence of a ring. If imaged from any point along the diffraction ring, the dark-field micrograph shows a high density of tiny particles of about 8 to 10 nm in the mean diameter (Figure 7(d)). Its corresponding bright-field micrograph at the same orientation of samples also exhibits the similar mottled background, as stated previously. However, these rings, tiny particles, and mottled background would disappear if samples were tilted several degrees away from the observed orientations. Furthermore, compared to Figure 8, the diffraction ring in Figure 7(c) passes ⟨025⟩$_{S'}$ **g** vectors which

are close to ⟨220⟩$_{Al}$. If the observed zone axes are near ⟨101⟩$_{Al}$, the ring of the same diameter could also be found, as shown in Figure 9(a). For a longer aging time, more rings would appear, which were also found in the 2024 alloy and at other aging conditions studied. The representative diffraction pattern is shown in Figure 9(b). In addition to the outer ring mentioned previously, the intermediate ring runs through ⟨200⟩$_{S'}$ **g** vectors and is close to ⟨200⟩$_{Al}$, and the inner ring runs through ⟨131⟩$_{S'}$ **g** vectors.

For the stretched Al-Cu-Mg alloy aged at 190 °C for 30 s the aging stage corresponds to the commencement of the sigmoidal portion in Figure 2. Figure 10(a) shows that numerous helical dislocations aligned along ⟨110⟩$_{Al}$ directions. Because the bright-field micrograph was taken with a given two-beam diffraction vector (**g** vector) to obtain a clear image of the dislocation morphology, only dislocations of some slip systems were visible according to the invisibility criteria (**g** · *b* = 0). If observed from other **g** vectors and/or at different zone axes, dislocations of other slip systems could also be found. The radii of these helical dislocations are much smaller than those of dislocation loops in Figure 6. As shown in Figure 10(b), a considerable number of tiny S' laths also have precipitated at this time, in contrast to the situation Figure 6. However, as shown in Figure 10(c), the radii of these helical dislocations do not appreciably increase with increasing the aging time up to 1 hour. Moreover, as shown in Figure 10(d), the morphology of tiny particles (GPB2 zones or the S" phase) is seen to be comparable with that for the unstretched specimen at the same aging condition.

b. Under-peak aging

For a longer aging time, the comparisons between the unstretched and stretched specimens are shown in Figure 11. For the unstretched specimens, a few S' laths could be appreciated from the dark-field image in Figure 11(a) to have precipitated on the pre-existing dislocation loops at the aging time of 3 hours, which corresponds to the beginning of the sigmoidal portion of the conductivity curve. Some of them exhibit the morphology of corrugated sheets (label A). On the other hand, the S' precipitates in the stretched specimens present the morphology of needles and are more abundant in quantity than those in the unstretched specimen (Figure 11(b)). The sizes of these S' needles are about 70 nm in length and 12.5 nm in diameter, which were estimated from the dark-field micrographs imaged from the S' characteristic diffraction points, *e.g.*, ⟨131⟩$_{S'}$ of variant 2 and 4 or variant 6 and 8 for two orthogonal side-on views of the S' precipitates and ⟨041⟩$_{S'}$ of variant 11 for their end-on view. The typical diffraction pattern with streaks can be simulated by DIFFRACT software (a commercial software of Visual Lab., Albuquerque, NM 87125) and is illustrated in Figure 8 to show 12 variants with the orientation relationship of {001}$_{S'}$ ∥ {120}$_{Al}$ and ⟨100⟩$_{S'}$ ∥ ⟨001⟩$_{Al}$. Consequently, all the **g** vectors for the S' (S) phase can be identified.

c. Peak aging and overaging

As shown in Figures 11(c) and (d), the amount of the S' precipitates rapidly increases with increasing the aging time until peak hardness is achieved (about 12 hours, *i.e.*, the inflection point of the conductivity curve) regardless of pre-age stretching (Figures 11(a) and (b)). However, the density and volume fraction of the S' precipitates are higher in the stretched specimen than in the unstretched one. This is con-
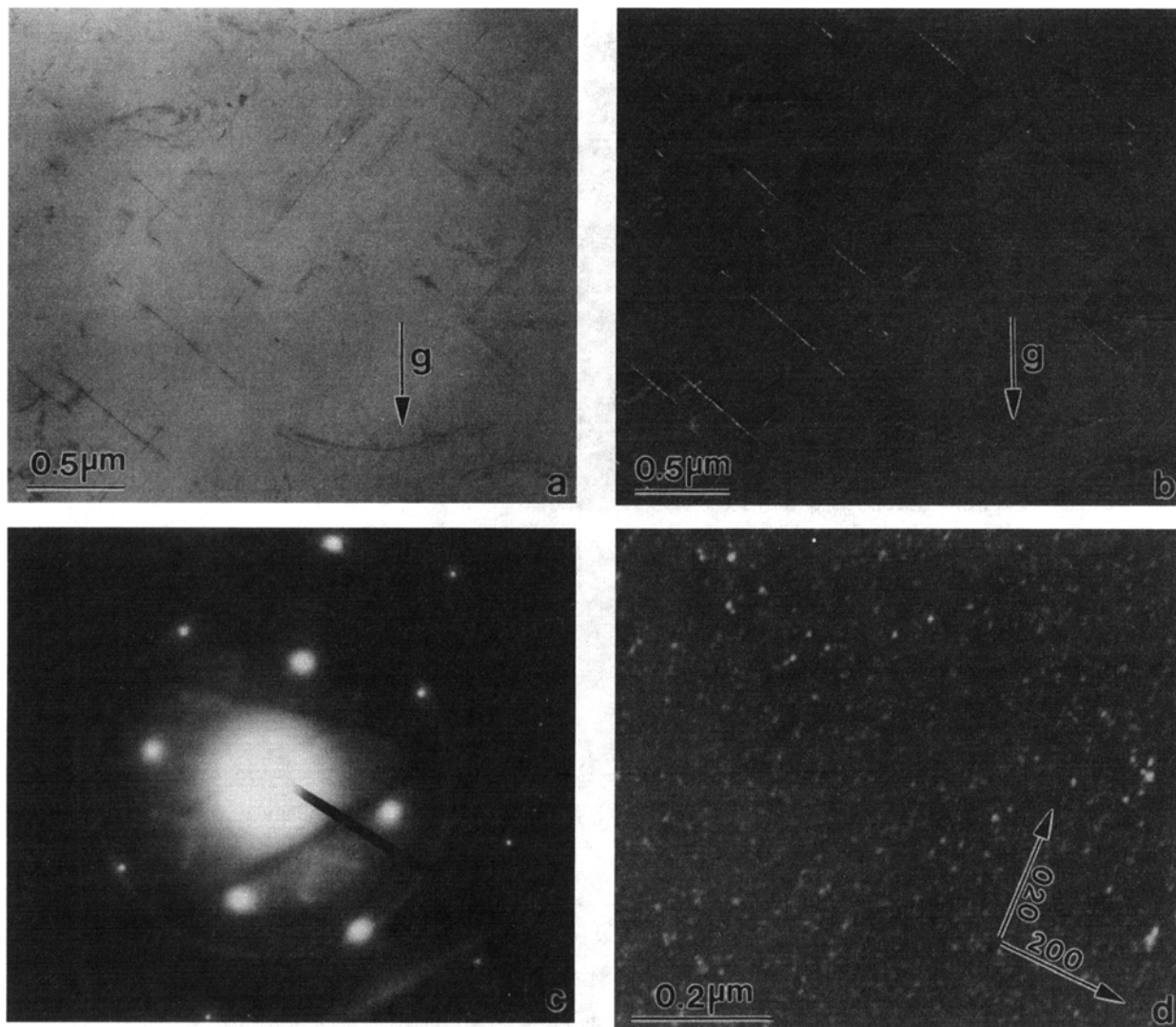
Fig. 7—Microstructure of the unstretched pseudobinary Al-Cu-Mg alloy aged at 190 °C for 1 h: (*a*) bright-field TEM micrograph (**g** = [0$\bar{2}$0]), showing single and paired dislocation loops growing in various orientations of {110}$_{Al}$ planes; (*b*) weak beam dark-field TEM micrograph (**g** = [020]) of (a), showing the decoration of very tiny S' precipitates on dislocation loops; (*c*) electron diffraction pattern, showing orthogonal and faint streaks, and a diffraction ring; and (*d*) dark-field TEM micrograph imaged from any point along the diffraction ring in (c), showing numerous tiny particles (GPB2 zones). All the TEM micrographs were taken near [001] zone axis.

sistent with the DSC results (curves 4 and 7 of Figure 5). On the other hand, the diameters of the discrete S' needles in the stretched specimen only become slightly coarser even though their lengths rapidly increase. The width and thickness of the discrete S' lath in the unstretched specimen also are much smaller than their length. As a consequence, it can be said that the S' phase basically remains a one-dimensional growth mode despite preage stretching. At the same time, the S' laths in the unstretched specimen were seen to gradually string together and coalesce with each other (label B), but the S' needles in the stretched specimen were not seen.

For a much longer aging time, the further variation in quantity of the S' precipitates is difficult to differentiate by TEM, even after 10 days, when the sigmoidal portion of the conductivity curve approaches a plateau, as shown in Figures 11(e) and (f). However, as shown in Figure 11(e), the coalescence between the S' (S) precipitates in the unstretched specimen aged for 10 days at 190 °C proceeds much completed (labels C and D), *i.e.*, the morphology of

most of the S' precipitates changes into wide plates, and the spacing among these S' plates becomes wider. On the other hand, the morphology of the S' (S) needles in the stretched specimen aged for 10 days still seems to be similar to that for 12 hours and were seen only slightly to merge among them. In addition, within cells which are the rectangular regions of the matrix encircled by the orthogonal S' plates, the number of mottled points remarkably decreases with increasing aging time from 12 h to 10 days, (compare Figure 11(c) with (e)).

For a very long aging time (*e.g.*, 20 days), the morphology of the S' (S) phase in the unstretched specimen basically remains unchanged. However, the coalescence between the S' (S) precipitates in the stretched specimen still can continue (Figure 12(a)), but to a lesser extent than that in the unstretched specimen under peak aging or overaging conditions (Figures 11(c) and (e)). At this time, the S' (S) diffraction points for the stretched specimen become sharper and the streaks become faint, as shown by comparing Figures 7(c), 8(a), 9, and 12(b).

○ : Matrix
⊙ : S1~S4: $[100]_S$ // $[100]_M$
◐ : S5~S8: $[100]_S$ // $[010]_M$
● : S9~S12: $[100]_S$ // $[001]_M$

A: $(1\bar{3}\bar{1})_{S6}$, $(\bar{1}3\bar{1})_{S8}$ E: $(0\bar{2}\bar{3})_{S10}$
B: $(\bar{1}1\bar{2})_{S5}$, $(\bar{1}1\bar{2})_{S7}$ F: $(0\bar{4}\bar{1})_{S12}$
C: $(\overline{112})_{S1}$, $(\bar{1}1\bar{2})_{S3}$ G: $(0\bar{4}\bar{1})_{S11}$
D: $(\bar{1}3\bar{1})_{S2}$, $(\bar{1}3\bar{1})_{S4}$ H: $(02\bar{3})_{S9}$
                                 I: $(02\bar{5})_{S9}$

Parameters for simulating S' (S) diffraction:
(1) orthorhombic structure
(2) a=4.00Å, b=9.23Å, c=7.14Å
(3) $\{001\}_S$ // $\{\bar{1}20\}_M$; $<100>_S$ // $<001>_M$
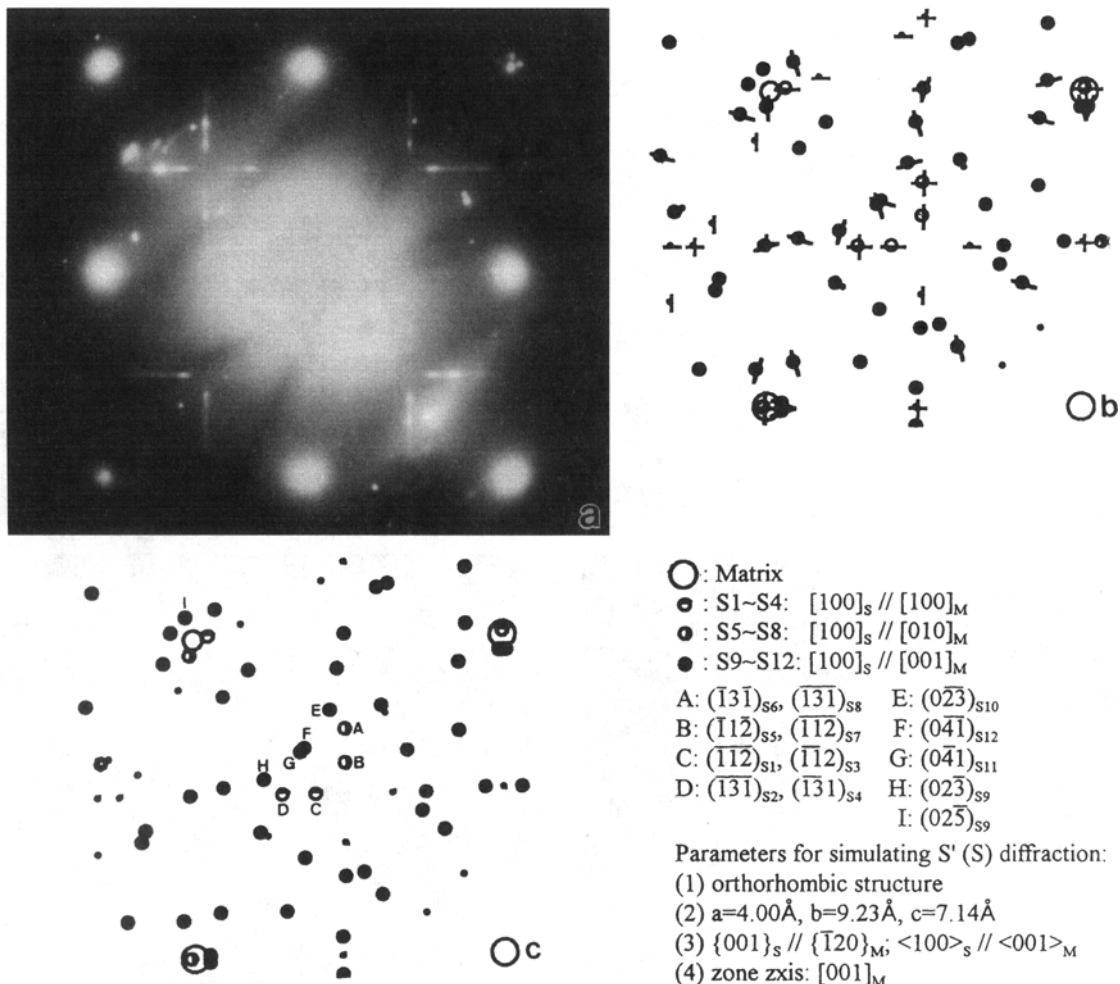(4) zone zxis: $[001]_M$

Fig. 8—(a) Typical electron diffraction pattern ($z \approx [001]$) of the pseudobinary Al-Cu-Mg or 2024 alloy aged at 190 °C for 12 h and up to about 10 days; (b) schematic diffraction pattern with streaks ($z = [001]$), simulated by DIFFRACT software; and (c) schematic diffraction pattern without streaks, showing diffraction points from 12 variants of the S' (S) phase. The parameters used for this simulation are included.

2. Commercial 2024 alloy

a. Aging at 190 °C

The morphology of the S' plates in the unstretched specimen of the 2024 alloy aged at 190 °C for 12 hours is similar to that of the Al-Cu-Mg alloy. However, the sizes of these plates in the former (Figure 13(a)) are obviously smaller than those in the latter (Figure 11(c)). In this figure, the mottled points similar to those observed in Figures 6(a) and (b) are visible as well within the cells encircled by the orthogonal S' plates. Similarly, the needlelike S' precipitates in the stretched 2024 alloy aged at the same condition (Figure 13(b)) also are shorter and more abundant than those in the stretched Al-Cu-Mg alloy (Figure 11(d)).

b. Aging at other temperatures

At other aging temperatures (170 °C and 240 °C), the variation of morphology of the S' phase is similar to that at 190 °C. Typical dark-field micrographs that were taken from the thin foils of the unstretched 2024 alloy aged at 240 °C for 1.5 hours are shown in Figures 14(a) and (b), which exhibit the end-on view (width and thickness) and side-on view (length) of the S' precipitates, respectively. From these two micrographs, the length of the S' precipi-tates is shown still to grow at a higher rate than the other two dimensions, even though specimens were overaged at a higher temperature of 240 °C. Moreover, the diameters of the tiny precipitates within the cells encircled by the S' precipitates (Figure 14(a)) are similar to those in the unstretched Al-Cu-Mg alloy aged at 190 °C for 1 hour (Figure 7(d)). However, the side-on view (Figure 14(b)) shows these tiny precipitates are cylindrical in morphology. This means that they basically grow in a one-dimensional mode along $\langle 001 \rangle_{Al}$ directions. The corresponding bright-field image is thus a mixture of the mottled points and cylinders. It was also found that most of these cylindrical precipitates still survive even after long-term overaging.

IV. DISCUSSION

A. Microstructures

1. Dislocation morphology

In the early stage of low-temperature aging, individual dislocation loops (Figures 6, 7(a), and 11(a)) and helical dislocations (Figures 10(a), 10(c), and 11(b)) appear in the matrix of the unstretched and stretched specimens, respectively. These dislocation loops result from the condensation and collapse of quenched-in vacancies on the adjacent
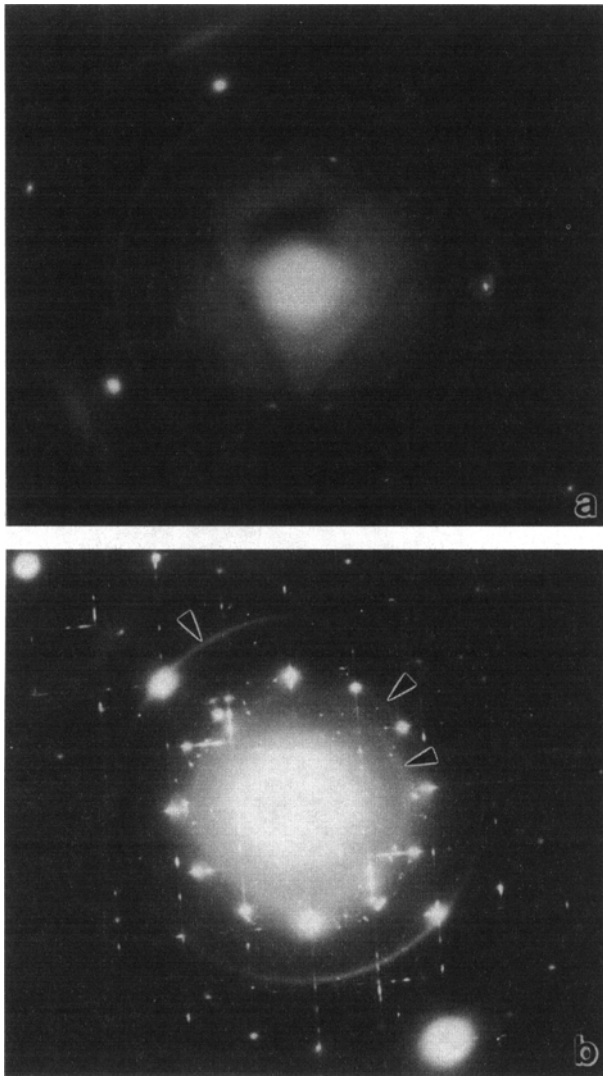
Fig. 9—Electron diffraction patterns of (a) the pseudobinary Al-Cu-Mg alloy aged at 190 °C for 1 hr ($z \approx$ [101]) and (b) the 2024 alloy aged at 190 °C for 64 h ($z \approx$ [001]). The outer, intermediate, and inner rings are indicated with arrows.

$\{110\}_{Al}$ planes and therefore they can grow when more vacancies are delivered to the interior of the loop. On the other hand, when quenched-in vacancies are diffused into the core of the screw dislocation to stimulate its climb, the helical dislocation is induced by producing, along the dislocation line, a number of edge dislocation steps perpendicular to the dislocation line vector.[5,6,25] Therefore, the radius of the helical dislocation also can increase in the same way as that of the dislocation loop. The increment in radii of these two kinds of dislocations thus may be regarded as an indication of a relative quantity of quenched-in vacancies residing in the matrix. For the unstretched specimens, the radii of the dislocation loops can continue to grow up to at least 3 hours (Figures 7(a) and 11(a)). This implies that a considerable number of free quenched-in vacancies are not tied up and thus can assist the growth of GPB and GPB2 zones.

However, for the stretched specimens, the radii of the helical dislocations are much smaller than those for the unstretched specimens (Figures 6 and 10(a)) and do not appreciably change with increasing aging time (Figure 10(c)).

This means that in the very early stage of aging (<30 minutes) free quenched-in vacancies had been widely exhausted by the climb of a large number of screw dislocations induced by preage stretching. Even so, the morphology and the amount (Figures 7(d) and 10(d)) of tiny particles (*i.e.*, GPB2 zones, as stated in Section IV–A–2) in the stretched specimens do not seem affected significantly by a large reduction of available quenched-in vacancies. This suggests that the role of quenched-in vacancies which assist the diffusion of solutes to speed up the nucleation and growth of GPB2 zones has been replaced by that of dislocation pipes due to preage stretching.

Wilson[6] attributed paired dislocation loops (Figure 6(b)) to the heterogeneous nucleation of partially coherent S' precipitates, which resolve a single dislocation line into double ones. Subsequently, these dislocation lines present the morphology of discontinuity in their WBDF image when the aging time slightly increases (Figure 7(b)). This is another indication of the initial precipitation of the S' phase onto dislocation lines, corresponding to the orthogonal streaks in the diffraction pattern (Figure 7(c)).

2. GPB and GPB2 zones

In addition to various types of dislocations, a mottled background (Figure 6) concurrently appears in the matrix in the early aging stage (*e.g.*, at 190 °C for 30 minutes). The mottled points also appear at peak aging and overaging stages (Figures 11(c) and (e)) and at the 2024 alloy (Figure 13(a)). Bonfield and Datta,[25] in their study on the Al-4Cu-0.8Si-0.8Mg alloy aged at room temperature and at 130 °C for up to 80 hours, reported that the mottled background resulted from the coherency strain field of GP1 and GPB zones. However, the mottled background was difficult to observe in the two alloys studied when they were aged at room temperature for four days or at 190 °C for 1.5 minutes. This is because these two alloys, under these aging conditions, nearly only contain GPB and/or GPB2 zones, which produce a smaller lattice strain than GP1 zones unless they grow to a critical size. Moreover, the GPB zone can transform rapidly *in situ* into another similar structure at the aging temperatures studied, according to the DSC results (curve 2 of Figure 5). This can correspond to the dilatometric work of Pysz and Tietz,[26] who reported that the volume of materials first expanded at the beginning of aging and then shrank during aging, exhibiting a process of atom clustering and then ordering. Saulnier and Syre[27] also suggested a similar conclusion but considered the ordering to be only partial. The mottled points observed in the present study thus can be attributed to the precipitation of GPB2 zones (or the S'' phase).

Furthermore, the corresponding dark-field micrographs of the mottled points show a high density of tiny particles (Figures 7(d) and 10(d)) as imaged from any point along one of the diffraction rings (Figures 7(c) and 9). The similar dark-field image also had been observed using TEM by Shchegolayev and Buynov,[16] who otherwise reported a similar ring pattern in their X-ray work for the same specimen. However, Silcock[14] only observed strong and broad X-ray diffraction points (*i.e.*, arcs) for the specimen subjected to a similar aging treatment. This is similar to the situation where the thin foil was tilted slightly from the observed orientations (Figure 9(b)). Obviously, the ring pattern does not result from either oxides or many fine grains
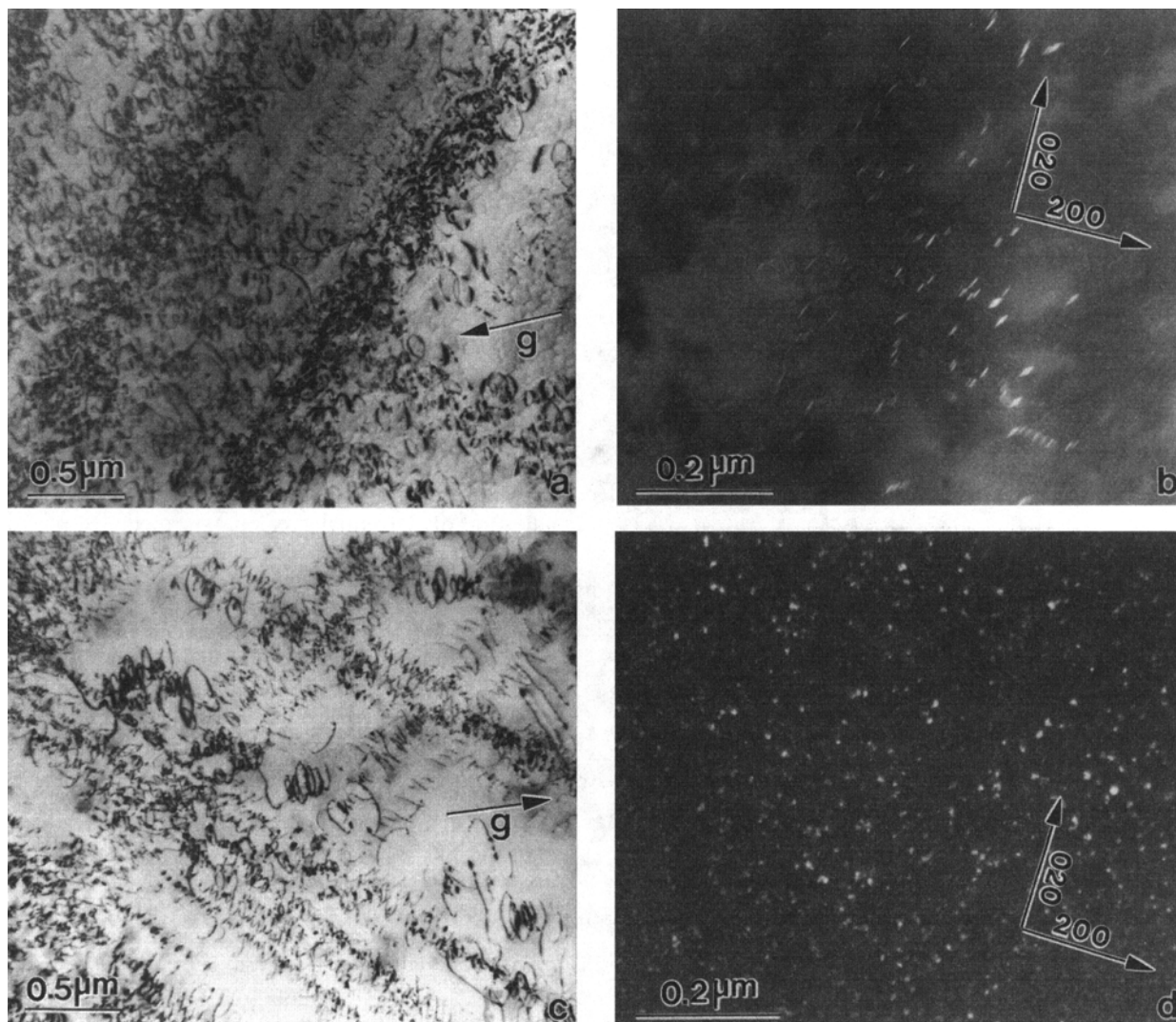
Fig. 10—Microstructure of the stretched (1.5 pct preaging strain) pseudobinary Al-Cu-Mg alloy aged at 190 °C for 30 min: (a) bright-field TEM micrograph ($\mathbf{g} = [\overline{2}00]$), showing arrays of helical dislocations aligned along $\langle 110 \rangle$ directions; (b) dark-field TEM micrograph imaged from $(0\overline{4}1)_{S'}$ of variant 11 and $(0\overline{4}1)_{S'}$ of variant 12, showing the end-on view of tiny S' precipitates in $\{120\}$ planes, and aged at 190 °C for 1 h; (c) bright-field TEM micrograph ($\mathbf{g} = [\overline{2}00]$), showing the variation of radii of helical dislocations; and (d) dark-field TEM micrograph imaged from any points along the diffraction ring, showing the appearance of tiny particles (GPB2 zones). All the TEM micrographs were taken near the [001] zone axis.

(here, grain size > 50 μm). It should result from an intermediate structure (GPB2 zones or the S″ phase) between GPB zones and the S' phase because GPB zones rapidly disappear within 1.5 min at 190 °C (curve 2 of Figure 5) and the ring pattern is distinguishable in morphology from the characteristic diffraction points of the S' phase. Although Bagaryatsky[28] and Shchegolayev and Buinov[16,29] proposed that this intermediate structure was the S″ phase, Silcock[14] reported that the structure of the precipitates corresponding to the current aging conditions was not related to that of the S″ phase and recognized it as GPB2 zones.

The correlation between the diffraction rings and the structures of GPB and GPB2 zones will be further elucidated. As suggested by Bagaryatsky,[30,31,32] the GPB zone consists of groups of atoms including a copper and a magnesium atom together with some aluminum atoms. The atom groups that lie on adjacent $\{100\}_{Al}$ planes shift from their equilibrium positions a relative horizontal distance to one another. In other words, they are statistically uniformly

arranged in the $\{100\}_{Al}$ planes and thus locally disturb the strict periodicity in the arrangement of the atoms with respect to the matrix lattice. Nevertheless, the continuity of the matrix lattice remains perfect in the $\langle 001 \rangle_{Al}$ directions. Similarly, the GPB2 zone should have a similar structural arrangement but different lattice parameters and be partially ordered, as stated previously. Therefore, the structure of GPB and GPB2 zones can be considered as a composite of a number of individual precipitate units, each of which randomly orients with respect to a common $\langle 001 \rangle_{Al}$ direction. This is analogous to a fiber texture exhibited by a cold-drawn wire whose grains have a preferred orientation with respect to the wire axis. As long as the d-spacing of a particular (hkl) plane satisfies the Bragg law, the reflecting beams from the same planes of these randomly oriented precipitate units will lie on the surface of a cone with apex angle $4\Theta_{(hkl)}$ centered on the incident beam direction and produce a ring when intersecting with the TEM film. However, the size and volume percentage of GPB or GPB2
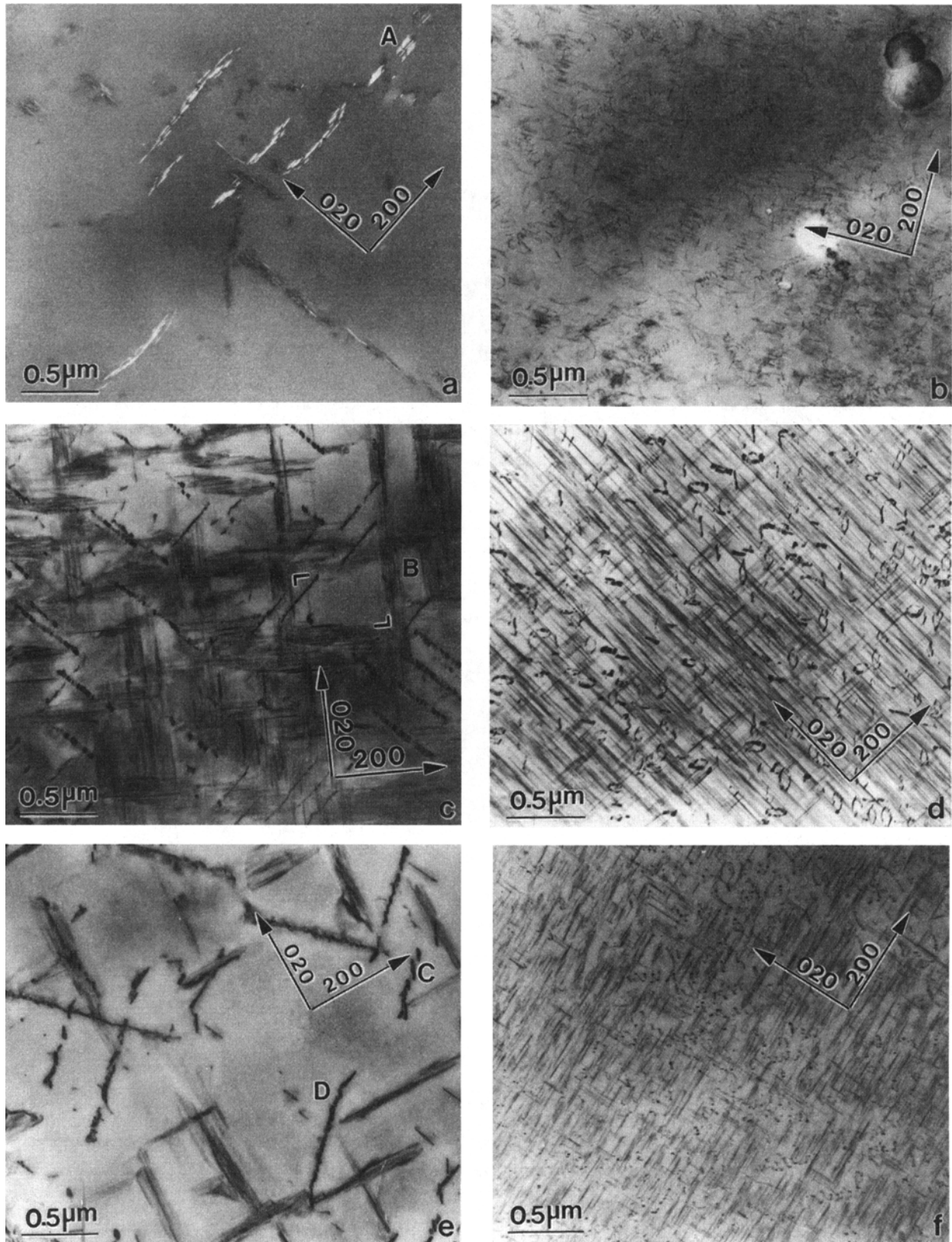
Fig. 11—Comparison of microstructures of the pseudobinary Al-Cu-Mg alloy aged at 190 °C for (a) and (b) 3 h (underaging), (c) and (d) 12 h (peak aging), and (e) and (f) 10 days (long-term overaging). (a), (c), and (e) unstretched specimens, showing corrugated S' sheets (at A) and the coalescing process of S' laths (e.g., at B, C, and D). (b), (d), and (f) stretched (1.5 pct preaging strain) specimens, showing numerous S' needles and least coalescence among them. All the bright-field TEM micrographs were taken near the [001] zone axis. A cell encircled by the S' precipitates is indicated, as bracketed in (c).
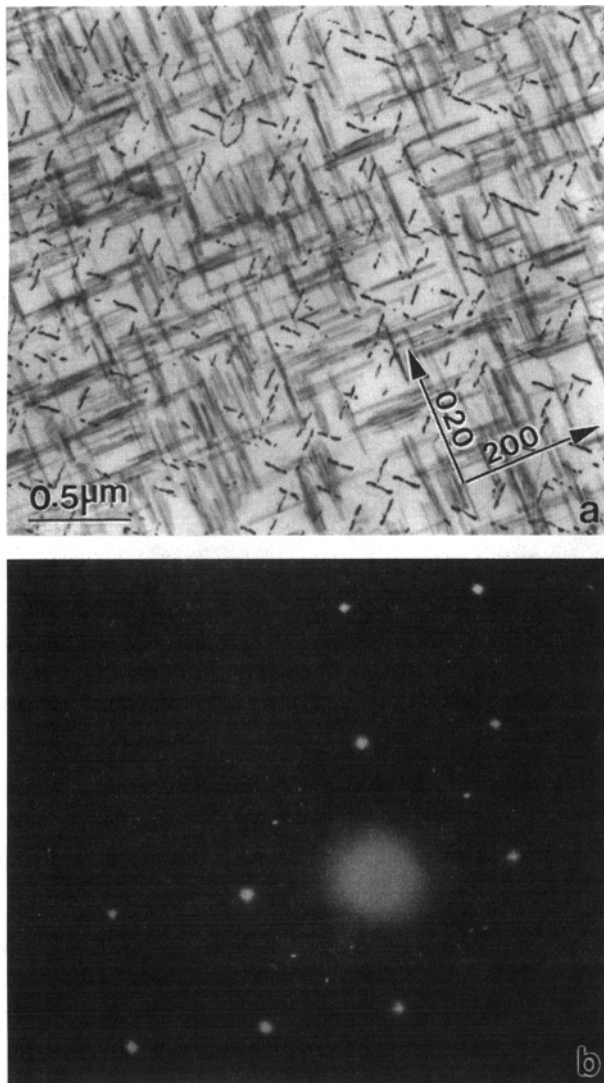
Fig. 12—(a) Microstructure and (b) diffraction pattern of the stretched (1.5 pct preaging strain) pseudobinary Al-Cu-Mg alloy aged at 190 °C for 20 days, showing the coalescence of S' (S) needles into laths and sharp S-phase diffraction points with very weak streaks. The bright-field TEM micrograph was taken near the [001] zone axis.
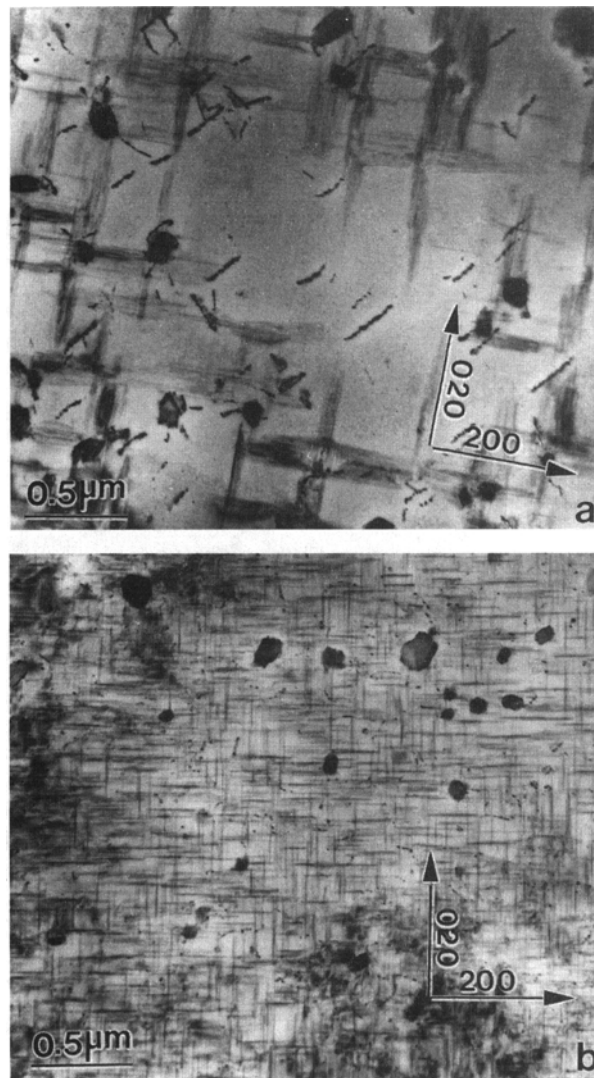

Fig. 13—Microstructures of the 2024 alloy aged at 190 °C for 12 h (peak aging): (a) bright-field TEM micrograph for the unstretched specimen, showing narrow and short S' plates, and (b) bright-field TEM micrograph for the stretched (1.5 pct preaging strain) specimen, showing thinner, shorter, and more S' needles. All the TEM micrographs were taken near the [001] zone axis.

zones alone also must be large enough to yield a complete ring and to reflect sufficient intensity.

As the sizes of the GPB2 zone, especially its length, increase with increasing aging time or the alloying contents, more rings which are weak in the structure factor also can be anticipated to appear (Figure 9). This is justified because the outer, intermediate, and inner rings shown in Figure 9(b) can be respectively identified as arising from the reflection of {025}, {023}, and {013} planes of GPB2 zones if the c-axis of the GPB zone is adjusted, i.e., $c' = 2c = 0.808$ nm (Bagaryatsky[30,31,32] identified the structure of the GPB zone to be a tetragonal cell with $a = 0.55$ and $c = 0.404$ nm). The reflection planes thus observed are in good agreement with those reported by Bagaryatsky, but not with those predicted from lattice parameters of GPB zones proposed by Mondolfo[15] (orthorhombic cell with $a = 0.405$, $b = 0.906$, and $c = 0.725$ nm). Again, this proves that the GPB2 zone has a similar crystal structure as the GPB zone but different lattice parameters. Moreover, the ring pattern

so far can be obtained only in two characteristic directions, i.e., near $\langle 001 \rangle_{Al}$ and $\langle 101 \rangle_{Al}$ (Figure 9). Together with the preceding observation about the lattice structure, this means that the in situ transformation of the GPB zone into the GPB2 zone may only be a "partially" ordered action of atom groups in the GPB zone. Consequently, based on these facts that diffraction rings reflect an ill-defined atom arrangement and the GPB2 zone is only a partially ordered version of the GPB zone, it seems more appropriate to describe the intermediate structure as the GPB2 zone rather than a phase (S"), in a similar manner to describe the GP2 zone rather than the θ" phase in Al-Cu alloys. This is corresponding to Silcock's description.[14]

As stated in Section IV–A–1, the growth of GPB2 zones can be enhanced by abundant quenched-in vacancies for the unstretched specimens, but by numerous dislocation pipes for the stretched ones. They basically follow one-dimensional growth mode. Therefore, after a short aging period,
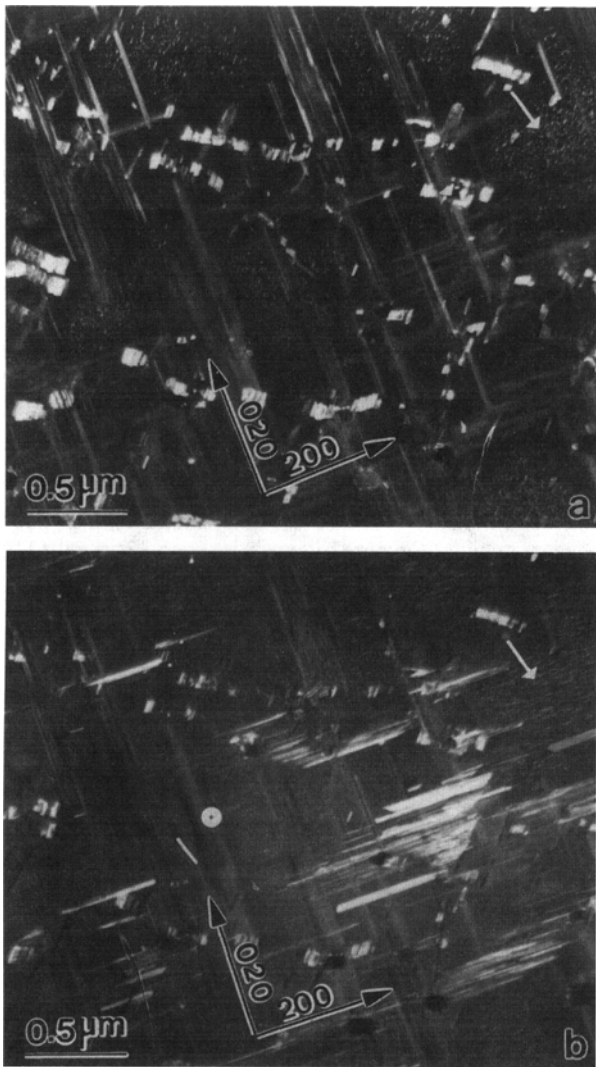
Fig. 14—Microstructures of the 2024 alloy aged at 240 °C for 1.5 (overaging): (a) dark-field TEM micrograph imaged from $(02\bar{3})_{S'}$ of variant 12 covering partial $(1\bar{3}1)_{S'}$ of variant 6, showing the end-on view (i.e., diameter) of the S' precipitates and GPB2 zones (tiny particles within cells encircled by S' plates, as arrowed); and (b) dark-field TEM micrograph imaged from $(1\bar{3}1)_{S'}$ of variant 2, showing the side-on view (i.e., length) of the S' precipitates and GPB2 zones (tiny cylinders within cells encircled by S' plates, as arrowed). All the TEM micrographs were taken near the [001] zone axis.

the length of these cylindrical GPB2 zones can quickly grow but their diameters no longer significantly increase (Figure 7(d), 11(c), 11(e), and 14(a)). This phenomenon can be rationalized according to the preceding analysis that the structure of the GPB2 zone is distinguishable from the GPB zone only by letting $c' = 2c$. As a consequence, the preferential axial growth of GPB2 zones can be attributed to both nearly no coherency strain and little interfacial energy increase in the c-direction, in contrast with a considerable expansion entirely perpendicular to the axis of the cylinder (the lattice parameters of the matrix are $a = 0.405$ nm and thus $2a = 0.810$ nm). Additionally, with the axial growth of GPB2 zones the resulting total strain does not significantly increase, which leads to the leveling of the conductivity and hardness curves. This phenomenon suggests that the decreased strain energy due to solute removing out of solid solution just

counterbalances the increased strain energy due to the increase in the volume fraction of GPB2 zones.

From the thermodynamics standpoint, the growth of GPB2 zones should completely cease when the precipitation of the energetically more favorable S' phase commences. However, few GPB2 zones still survive long-term overaging (curve 5 of Figure 5 and Figures 6, 7, 11, and 14). This involves the relative phase stability of GPB2 zones to the S' precipitates and the dissolution kinetics of these zones. Indeed, the C peak in Figure 5 spans a wide temperature range, suggesting that a distribution in size of GPB2 zones exists (Figures 6(a), 7(d), and 10(d)). As a consequence, tiny S' precipitates initially nucleated can grow at the expense of most subcritical-sized GPB2 zones, which are thermodynamically more unstable. However, few critical-sized GPB2 zones that are relatively stable (metastable) to subcritical-sized GPB2 zones and S' precipitates can still continue to grow due to the Gibbs–Thomson (capillarity) effect. Up to a much longer aging time, the capillarity effect vanishes due to the accelerating growth of all the S' precipitates over a critical size. Accordingly, the coarsened (especially in length) S' (or S) precipitates eventually attack and gradually consume large-sized metastable GPB2 zones, as well (Figure 11(e)). This situation was more pronounced as dislocations were introduced to assist the growth of the S' precipitates (Figure 11(f)).

3. S' (S) phase

The initial formation of the S' phase can be revealed by double (Figure 6) and discontinuous dislocation lines (Figure 7(b)), as stated in Section IV–A–1. Based on the experimental results in Figures 7(a), 7(b), 11(a), and 11(b), the S' phase was believed to preferentially precipitate on dislocations, though GPB and GPB2 zones also were considered as the precursors of the S' phase.[33,34] Therefore, the S' precipitates become more closely spaced and thinner when preage stretching was applied to introduce numerous dislocation lines for the nucleation. The precipitation planes of the S' phase were also found to be $\{120\}_{Al}$ (Figures 10(b) and label C of Figure 11(e)) and its growth directions to be $\langle 100 \rangle_{Al}$ (Figures 11 through 14). This is in agreement with results reported by many investigators.[15,35] Therefore, the diffraction pattern (Figure 8) resulting from the twelve variants of the S' precipitates could be simulated by DIFFRACT software according to the previously mentioned orientation relationship with the matrix. The first 8 of these 12 variants of S' were similarly depicted by Gupta et al.[35] as well.

For the unstretched specimens, the growth of the S' precipitates proceeds in two morphologies, i.e., corrugated sheets and wide plates. As suggested by Wilson and Partridge,[12] these corrugated S' sheets (label A in Figure 11(a)) stem from the interaction of dislocation loops and the S'-induced strain field. They precipitate on two energetically favorable $\{210\}_{Al}$ planes within the dislocation loops and grow along $\langle 001 \rangle_{Al}$ directions, thus forming a composite S' (S) sheet on $\{110\}_{Al}$ planes. Moreover, Radmilovic et al.[34] observed the thickening of the S' precipitates by the ledge migration using high-resolution electron microscopy (HREM). On the basis of these facts, the formation of the corrugated S' sheets can be schematically illustrated in Figure 15(a) as the combination of the modes proposed by Wilson and Partridge and Radmilovic et al.
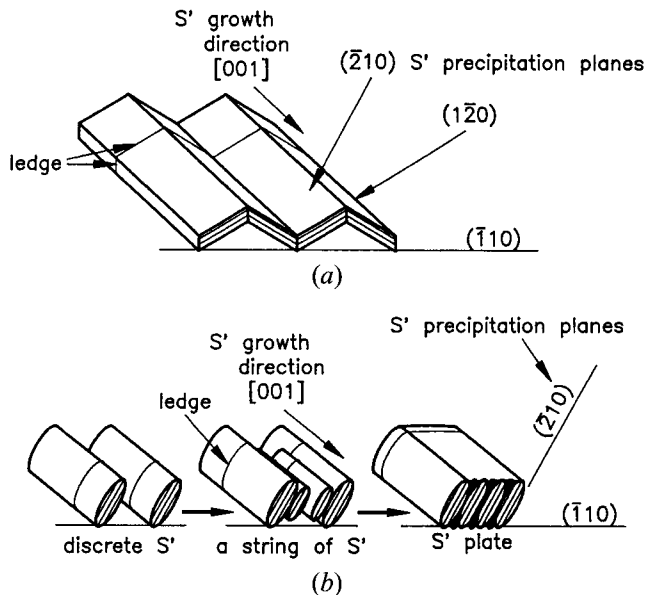
Fig. 15—Schematic diagrams of two alternative coalescing modes on {110} planes, of S' laths precipitating on {120} planes and growing along ⟨001⟩: (a) S' laths in energetically favorable two of adjacent {120} planes merge into corrugated precipitate sheets (corresponding to label A in Fig. 11(a))[12] and thicken along ⟨210⟩ by the ledge mechanism;[34] and (b) discrete S' laths on same {120} planes first string and then merge into plates (corresponding to label B in Fig. 11(c) and labels C and D in Fig. 11(e)) and also thicken along ⟨210⟩ by the ledge mechanism.

Alternatively, the S' precipitates can coalesce each other into wide plates on {110}$_{Al}$ planes by the nucleation and growth of new S' laths along the interface of the previously formed ones and also thicken by the ledge mechanism. Here, the S' laths lie on adjacent and parallel planes, in contrast to adjacent but not parallel planes in the preceding case. The nucleation of these new S' laths may arise from the composition gradient established at the interphase boundaries between the S' precipitates and the matrix or from a smaller interphase interfacial energy. Therefore, the coalescing steps also can be schematically shown in Figure 15(b) and corresponded to label B in Figure 11(c), as well as labels C and D in Figure 11(e). Furthermore, because the number of nucleation sites increases due to preage stretching, the S' precipitates remain discrete until a very long aging time (e.g., >10 days) when they then gradually coalesce into laths (Figure 12(a)).

When comparing the TEM end-on and side-on view images of the discrete S' precipitates in the early and late stages of aging (Figure 11), it is noticed that the growth rate of the S' phase along its a-axis is much larger than that along the other two crystal axes (i.e., needle shape). For this growth anisotropy, Wilson and Partridge[12] defined a parameter, termed the matching periodicity p, which is the number of aluminum lattice planes corresponding to one lattice spacing of the S' phase. The p values along a-, b-, and c-axes of the S' phase are thus 0.99, 10.2, and 7.9, respectively. Therefore, the interfaces between the S' phase and the matrix remain coherent along the a-axis with little elastic strain, but lose coherency along the other two axes due to the large periodicity. As a result, assuming that the interfacial energy of a lattice plane is approximately proportional to the p values along both the axes constructing

this plane, Wilson and Partridge concluded the difference in the relative interfacial energy of the lattice planes perpendicular to these three axes determined the equilibrium shape of the S' phase. From the viewpoint of energy, this only explains the fact in part. This is because during the growth of precipitates, the effect of the volume-free energy change for two sequent transition phases, even if only a fraction of that for the overall transformation, is usually considerably larger than those of the interfacial and strain energies. Recalling the phase transformation theory,[36] it is realized that the incoherent interface has a much higher accommodation factor (i.e., mobility) than the coherent or semicoherent interfaces. Accordingly, the large difference in the interface mobility (i.e., the relative migration rate) along these three axes should be the predominating factor responsible for the final equilibrium shape of the S' phase.

The volume fraction of the S' precipitates under the same aging condition, e.g., 190 °C × 12 hours, increases due to preage stretching (compare Figures 11(c) and 13(a) with 11(d) and 13(b)) and higher alloying contents (compare Figure 11(d) with 13(b)). This can be complementally proved by the DSC results (curves 4 and 7 of Figure 5). In addition, the spacing, thickness, and length of the S' plates decrease due to the addition of Si (compare Figures 11(c) and (d) with 13(a) and (b)). This is because silicon can increase the nucleation density of the S' precipitates.[5,12] Also, it can increase the interfacial energy of the S' phase and thus lower its growth rate, especially in the axial direction.[12]

As shown in Figure 5, no definite S precipitation peak existing in DSC thermograms implies the in situ transformation of the S' phase into the S phase. This confirms the viewpoint of Silcock[14] and Gupta et al.,[35] that is, the S' phase is only a slightly distorted version of the S phase. Therefore, the crooked S-phase spots and streaks joining these spots, which all represent the precipitation of the S' phase, exist in X-ray[14] and TEM diffraction patterns (Figures 7(c), 8(a), and 9(b)) during most of the aging stages. The sharp S phase spots can be seen only in the stage of very long-term overaging (Figure 12(b)).

B. Conductivity, Hardness, and Aging Sequence

For the two alloys studied, the decrease of conductivity with preage stretching is trivial in the as-quenched state (<0.8 pct IACS) as well as the leveling portion (<0.5 pct IACS) and is only appreciable in the plateau (<2 pct IACS). According to the microstructural examinations, this suggests, in turn, that the conductivity is not sensitive to the variations of dislocations, quenched-in vacancies and the precipitate morphology. Consequently, together with the DSC result, the initial descending, leveling, and sigmoidal portions of the conductivity curve can be mainly attributed to the precipitation of GPB zones, GPB2 zones, and the S' phase, respectively. Additionally, the products aging under room temperature can be inferred to be GPB and/or GPB2 zones, based on the Rosen and Horowitz result that the conductivity no longer significantly changes after initial descending.[20]

The aging time required for the initial descending in conductivity decreases from 10³ min at room temperature (Figure 1 in Reference 20) to a few minutes at the aging temperature of 170 °C, indicating that the initial descending rate rapidly increases with the aging temperature. However,

this rate remains virtually unchanged within the temperature range between 170 °C to 190 °C and finally decreases when further increasing the aging temperature to 240 °C. Obviously, the precipitation of GPB zones is a thermally activated process involving the diffusion of Cu and Mg elements. The nose of the C curve for the precipitation of GPB zones can be deduced to situate between 170 °C and 190 °C as a result of an optimal compromise between the supersaturation and diffusivity of the solute atoms.
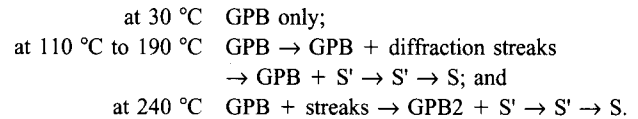
Similarly, the precipitation of GPB2 zones and the S' phase also are thermally activated processes since the positions of the leveling and sigmoidal portions of the conductivity curve change with the aging temperature. Therefore, for the unstretched Al-Cu-Mg alloy (Figure 1), the hardness corresponding to the leveling portion is lower at 240 °C than at the other aging temperatures studied, indicating a smaller amount of GPB2 zones and hence less lattice distortion (*i.e.*, higher conductivity). Under this aging temperature, the corresponding hardness for the stretched Al-Cu-Mg alloy (Figure 2) is similar to that for the unstretched, again indicating that the introduced dislocations do not affect the precipitation of GPB2 zones, as elucidated in Section IV–A–1. The initial drop in hardness (Figure 2) thus can be attributed to a stronger dislocation rearrangement due to recovery at higher temperature. However, this phenomenon does not occur in the stretched 2024 alloy because high-alloying contents facilitate the faster and greater precipitation of GPB2 zones (Figure 4), which also leads to a lower value of conductivity, as compared with the stretched Al-Cu-Mg alloy (Figure 2).

Corresponding to the S' precipitation, the slope of the sigmoidal portion from the beginning to the inflection point (*i.e.*, the maximum reaction rate) is an increasing function of time in contrast to a decreasing function of that from the inflection point of plateau. Therefore, these two regimes represent the accelerating and decelerating growth processes of the S' precipitates, respectively. In addition, the S' precipitation has already finished though the conductivity does not arrive at the final saturation value yet (Figure 1 and curve 5 of Figure 5). This suggests that the latter stage of the decelerating growth process of the S' precipitates is actually an Ostward ripening process. As the S' precipitates become thinner and more closely spaced, the diffusion fields of solute atoms overlap earlier. The overaging rate of the S' precipitates thus becomes slower (Figure 11), leading to the flattened peak hardness (Figures 2 and 4).

Looking at the beginning point of the sigmoidal portion, the S' precipitation can be appreciated to accelerate by both increasing alloying contents and preage stretching, but the effectiveness of the latter is larger than that of the former (Figures 1 through 3). This implies that dislocation lines provide nucleation sites for the S' precipitation more preferentially than GPB2 zones though both are available.[33,34]
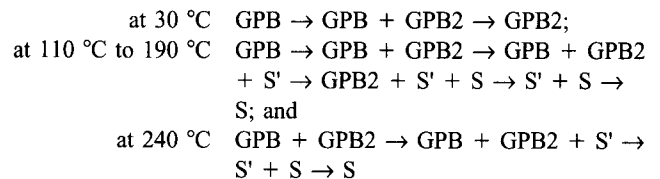
The patterns of the age-hardening curves obtained in this study, such as the shape of curves, the relative magnitude and position of peak hardness, and the number of the aging stage, *etc*, are in good agreement with Hardy's results[13] for an Al-Cu-Mg alloy with the Cu:Mg weight ratio of 2.2:1. In addition, following the age-hardening curves constructed by Hardy,[13] Silcock[14] has examined with X-rays the corresponding microstructural variations of the unstretched specimens of an Al-Cu-Mg alloy with the same Cu:Mg weight ratio as in

the alloy used in the present work. The results obtained led Silcock to propose the following aging sequence:

at 30 °C GPB only;
at 110 °C to 190 °C GPB → GPB + diffraction streaks
→ GPB + S' → S' → S; and
at 240 °C GPB + streaks → GPB2 + S' → S' → S.

Silcock[14] distinguished GPB2 zones causing strong and broad spots from an unidentified phase causing the streaks in the diffraction patterns. However, no additional precipitation peaks was observed between either the B and C peaks or between the C and D peaks in the DSC thermogram of the Al-Cu-Mg alloy used in the present work (Figure 5). The situation is similar to that during aging at other temperatures (170 °C and 240 °C). The S" phase and its diffraction pattern also have not been found in our TEM and Silcock's X-ray studies. Obviously, GPB zones transformed rapidly *in situ* into GPB2 zones and no phase other than the S' phase precipitates immediately after GPB2 zones. Moreover, as stated previously, GPB2 zones can exist at higher temperatures (Figure 14) and survive long-term overaging (Figure 11(e)). Therefore, the precipitates corresponding to broad spots and diffraction streaks in X-ray micrographs[14] can all be called GPB2 zones, and there only exists a difference among their sizes.

The formation of GPB and GPB2 zones and the S' (S) phase has been discussed previously. It must be restated here that after room-temperature aging for a considerable period, the existing transition phase will only be GPB2 zones and that during low-temperature overaging, few GPB2 zones can coexist with the S' phase and even the S phase (curves 5 and 6 of Figures 5 and 11(e)). Consequently, the aging sequence, based on the present study, can be revised as follows,

at 30 °C GPB → GPB + GPB2 → GPB2;
at 110 °C to 190 °C GPB → GPB + GPB2 → GPB + GPB2
+ S' → GPB2 + S' + S → S' + S →
S; and
at 240 °C GPB + GPB2 → GPB + GPB2 + S' →
S' + S → S

V. CONCLUSIONS

1. Based on the present analyses from hardness, conductivity, DSC, and TEM, the isothermal aging reactions of the pseudobinary Al-Cu-Mg alloy and the commercial 2024 alloy can be subdivided into five main stages as follows: (1) GPB zone precipitation, (2) fast *in situ* precipitation of GPB2 zones from GPB zones and their subsequent growth, (3) fast nucleation and accelerating growth of the S' phase, (4) decelerating growth of the S' phase, and (5) Ostward ripening of the S' and S phases.
2. Accompanying the precipitation of GPB2 zones, the electron diffraction ring pattern appears in two characteristic beam directions (near $\langle 001 \rangle_{Al}$ and $\langle 101 \rangle_{Al}$) and the number of rings increases with the axial growth of these zones (*i.e.*, increasing the aging time or alloying contents). On the diffraction analysis and the DSC result, it is suggested that the atom groups constructing the GPB or GPB2 zone cylinder are statistically uni-

formly arranged in the adjacent $\{100\}_{Al}$ planes and the GPB2 zone is only a partially ordered version of the GPB zone in a $\langle 001 \rangle_{Al}$ direction. The production of diffraction rings is analogous to a fiber texture of polycrystals in a cold-drawn wire.

3. From the thermodynamics standpoint, the growth of GPB2 zones should completely cease when the precipitation of the energetically more favorable S' phase commences. However, few over-critical-sized metastable GPB2 zones can still continue to grow and survive longterm overaging due to the Gibbs–Thomson (capillarity) effect and the dissolution kinetics.

4. The preferential nucleation of the S' precipitates on dislocations can be revealed by the dissociation (paired dislocation loops) and the discontinuity of dislocation lines (in the WBDF image). For the unstretched specimens, the S' precipitates subsequently grow and coalesce into two morphologies (corrugated sheets and wide plates). However, with the increase of nucleation sites introduced by preage stretching, this coalescing process does not occur until longterm overaging. Therefore, the rate of Ostward ripening decreases and the peak hardness becomes flattened.

5. The effects of alloying contents and preage stretching on the precipitation of the S' phase must be discriminated in terms of quantity and morphology of the precipitate. The former mainly exists in increasing its volume fraction. However, the nucleus density and thus the nucleation rate for the precipitation of the S' phase are more strongly stimulated by applying preaging strain than by increasing alloying contents.

6. In nature, the growth of the GPB2 zone and the S' phase roughly remain one-dimensional growth modes irrespective of the aging temperature and time or the preage stretching. The reason for the growth anisotropy is the minimization of the coherency strain for the GPB2 zone but is the differences in interfacial energy and relative mobility between coherent and incoherent interfaces for the S' phase.

7. For the stretched specimens, free quenched-in vacancies had been widely exhausted in the very early stage of aging by the climb of a large number of introduced screw dislocations, in contrast with the unstretched ones. However, the morphology and the amount of GPB2 zones seem similar for these two kinds of specimens. This suggests that the role of quenched-in vacancies in assisting the diffusion of solutes is replaced by that of dislocation pipes due to preage stretching.

8. The main factors affecting the electrical conductivity exist in the precipitation of redissolution of solute atoms. The effects of microstructural defects (vacancies and dislocations) are limited, as is that of the precipitate morphology as long as their sizes are not comparable to the scale of the mean free path of electrons.

ACKNOWLEDGMENTS

REFERENCES

1. T.H. Sanders, Jr. and E.A. Starke, Jr.: *Metall. Trans. A*, 1976, vol. 7A, pp. 1407-18.
2. G.M. Ludtka and D.E. Laughlin: *Metall. Trans. A*, 1981, vol. 12A, pp. 2083-91.
3. G.M. Ludtka and D.E. Laughlin: *Metall. Trans. A*, 1982, vol. 13A, pp. 411-25.
4. J.T. Vietz and I.J. Polmear: *J. Inst. Met.*, 1966, vol. 94, pp. 410-19.
5. R.N. Wilson, D.M. Moore, and P.J.E. Forsyth: *J. Inst. Met.*, 1967, vol. 95, pp. 177-83.
6. R.N. Wilson: *J. Inst. Met.*, 1969, vol. 97, pp. 80-86.
7. N. Sen and D.R.F. West: *J. Inst. Met.*, 1969, vol. 97, pp. 87-92.
8. F.S. Lin, S.B. Chakrabortty, and E.A. Starke, Jr.: *Metall. Trans. A*, 1982, vol. 13A, pp. 401-10.
9. F.G. Ostermann and W.H. Reimann: ASTM STP 467, ASTM, Philadelphia, PA, 1970, pp. 169-87.
10. F. Ostermann: *Metall. Trans.*, 1971, vol. 2, pp. 2897-2902.
11. M.C. Chaturvedi, D.W. Chung, and R.A. Doucette: *Met. Sci.*, 1979, pp. 34-38.
12. R.N. Wilson and P.G. Partridge: *Acta Metall.*, 1964, vol. 13, pp. 1321-27.
13. H.K. Hardy: *J. Inst. Met.*, 1954-55, vol. 83, pp. 17-34.
14. J.M. Silcock: *J. Inst. Met.*, 1960-61, vol. 89 pp. 203-10.
15. L.F. Mondolfo: *Aluminum Alloys: Structure and Properties*, Butterworth and Co., Boston, MA, 1976, pp. 497-505.
16. T.V. Shchegolayev and N.N. Buynov: *Fiz. Met. Metalloved.*, 1967, vol. 23, pp. 1026-32.
17. R. Horiuchi and Y. Minonishi: *J. Jpn. Inst. Met.*, 1970, vol. 39, pp. 936-43.
18. W.V. Youdelis and W. Fang: *Science and Engineering of Light Metals*, Japan Institute of Light Metals, Tokyo, 1991, pp. 917-22.
19. T. Croucher and D. Butler: *Heat Treating of Light Metals*, Japan Institute of Light Metals, Tokyo, 1983, pp. 18-19.
20. M. Rosen and E. Horowitz: *Mater. Sci. Eng.*, 1982, vol. 53, pp. 191-98.
21. A.K. Jena, A.K. Gupta, and M.C. Chaturvedi: *Acta Metall.*, 1989, vol. 37, pp. 885-95.
22. P.L. Rossiter and P. Wells: *Phil. Mag.*, 1971, vol. 24, pp. 425-36.
23. Richard Delasi and Philip N. Adler: *Metall. Trans. A*, 1977, vol. 8A, pp. 1177-83.
24. H.D. Chandler and J.V. Bee: *Acta Metall.*, 1987, vol. 35, pp. 2503-10.
25. W. Bonfield and P.K. Datta: *J. Met. Sci.*, 1976, vol. 11, pp. 1661-66.
26. G. Pysz and I. Tietz: *Neue Hüttz*, 1968, vol. 13, pp. 432-34.
27. A. Saulnier and R. Syre: *Rev. Met.*, 1952, vol. 49, p. 1.
28. Yu. A. Bagaryatsky: *Dokl. Akad. Nauk SSSR*, 1952, vol. 87, p. 397.
29. T.V. Shchegoleva and N.N. Buinov: *Sov. Phys.-Crystallogr.*, 1968, vol. 12, pp. 552-55.
30. Yu.A. Bagaryatsky: *Z. Tekhn. Fiz.*, 1948, vol. 18, p. 827.
31. Yu.A. Bagaryatsky: *Z. Tekhn. Fiz.*, 1950, vol. 20, pp. 424-27.
32. Yu.A. Bagaryatsky: *Dokl. Akad. Nauk*, 1952, vol. 87, p. 559.
33. G.C. Weatherly: Ph.D. Thesis, University of Cambridge, Cambridge, United Kingdom, 1966.
34. V. Radmilovic, G. Thomas, G.J. Shiflet, and E.A. Starke, Jr.: *Scripta Metall.*, 1989, vol. 23, pp. 1141-46.
35. A.K. Gupta, P. Gaunt, and M.C. Chaturvedi: *Phil. Mag.*, 1987, vol. 55, 375-87.
36. D.A. Porter and K.E. Easterling: *Phase Transformations in Metals and Alloys*, 1st ed., Pergamon Press, Oxford, United Kingdom, 1981.